

FILTERED TRACTOGRAPHY

A Thesis Proposal
Presented to
The Academic Faculty

by

James G. Malcolm

In Partial Fulfillment
of the Requirements for the Degree
Doctor of Philosophy in the
Electrical and Computer Engineering

Georgia Institute of Technology
9 October 2009

FILTERED TRACTOGRAPHY

Approved by:

XXX, Committee Chair
Electrical and Computer Engineering
Georgia Institute of Technology

Yogesh Rathi, Advisor
Electrical and Computer Engineering
Georgia Institute of Technology

Anthony Yezzi
Electrical and Computer Engineering
Georgia Institute of Technology

Allen Tannenbaum
Electrical and Computer Engineering
Georgia Institute of Technology

Date Approved: Not Yet Approved

TABLE OF CONTENTS

| | |
|--|----|
| SUMMARY | iv |
| I RESEARCH TOPIC | 1 |
| 1.1 Introduction | 1 |
| 1.2 Filtered Tractography | 3 |
| 1.2.1 Modeling local fiber orientations | 5 |
| 1.2.2 Estimating the fiber model | 7 |
| 1.2.3 The algorithm | 11 |
| II PRELIMINARY RESULTS | 13 |
| 2.1 Signal reconstruction and angular resolution | 15 |
| 2.2 Synthetic tractography | 17 |
| 2.3 <i>In vivo</i> tractography | 18 |
| III PROPOSED RESEARCH | 25 |
| 3.1 Work Completed | 25 |
| 3.2 Work Remaining | 25 |
| REFERENCES | 27 |

DISCLAIMER STATEMENT

Section 1 (background/literature survey) of this proposal was prepared without input from my research advisor or any other person. While technical writing guides may have been referred to, I did not solicit or receive assistance from any other person while preparing this portion of this document.

Signed  (student)

JAMES MALCOLM
(print name)

Approved:  (research advisor)

YOGESH RATHI
(print name)

SUMMARY

Computer vision encompasses a host of computational techniques to process visual information. Medical imagery is one particular area of application where data comes in various forms: X-rays, ultrasound probes, MRI volumes, EEG recordings, NMR spectroscopy, etc. This thesis proposal is concerned with techniques for accurate reconstruction of neural pathways from diffusion magnetic resonance imagery (dMRI).

This proposal introduces a filtered approach to neural tractography. Existing methods independently estimate the diffusion model at each voxel so there is no running knowledge of confidence in the estimation process. We propose using tractography to drive estimation of the local diffusion model. Toward this end, we formulate fiber tracking as recursive estimation: at each step of tracing the fiber, the current estimate is guided by those previous.

We show preliminary results using a mixture of Watson directional functions to model the diffusion signal. Compared to conventional techniques, this filtered approach significantly improves the angular resolution at crossings and branchings. Further, we confirm its ability to trace through regions known to contain such crossing and branching while providing inherent path regularization.

Future work will extend the technique to various alternative diffusion models and methods of tracing, as well as techniques for the analysis of tracts and validation of connectivity.

CHAPTER I

RESEARCH TOPIC

1.1 *Introduction*

The advent of diffusion weighted magnetic resonance imaging has provided the opportunity for non-invasive investigation of neural architecture. Using this imaging technique, neuroscientists can determine how neurons originating from one region connect to other regions and how well-defined those connections may be. For such studies, the quality of the results relies heavily on the chosen fiber representation and the method of reconstructing pathways.

To begin studying the microstructure of fibers, we need a model to interpret the diffusion weighted signal. Such models fall broadly into two categories: parametric and nonparametric. One of the simplest parametric models is the diffusion tensor which describes a Gaussian estimate of the diffusion orientation and strength at each voxel. While robust, this model can be inadequate in cases of mixed fiber presence or more complex orientations [3,14]. To handle more complex diffusion patterns, various parametric models have been introduced including mixtures of tensors [1, 25, 35, 36, 46] and directional functions [23, 31, 40]. To demonstrate the difference that arises, Figure 1 shows a tracing from the center of the corpus callosum. While a single-tensor model finds only the dominant U-shaped structure, multi-fiber methods reveal many of the lateral pathways known to exist.

Nonparametric models often provide more information about the diffusion pattern. Instead of estimating a discrete number of fibers as in parametric models, nonparametric techniques estimate an oriented distribution function (ODF) describing an arbitrary configuration of fibers. For this estimation, [45] introduced Q-ball

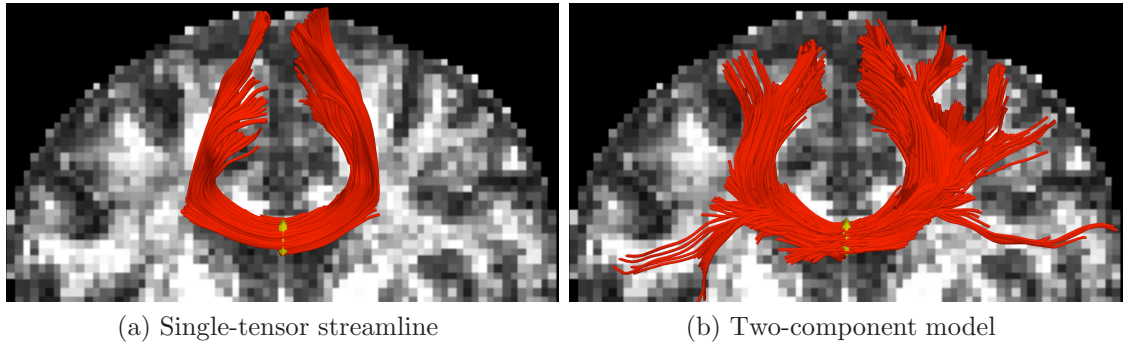


Figure 1: Comparison of tractography using a single-tensor model and the proposed two-component model with filtering. While the single-tensor model misses many of the lateral branches from the corpus callosum, the filter provides a stable estimate of the two-component model capable of revealing the lateral transcallosal pathways. Seed region indicated with yellow.

imaging to numerically compute the ODF via the Funk-Radon transform, and subsequently, the use of spherical harmonics simplified the computation with an analytic form [4, 10, 18]. Recently, linear Kalman filtering was demonstrated for online direct estimation of single-tensor and harmonic coefficients [9, 38]. Another approach to producing an ODF is to assume a model for the signal response of a single-fiber and use spherical deconvolution [20, 21, 23, 26, 44]. Diffusion oriented transforms offer even another alternative [32]. A good review of both parametric and nonparametric models can be found in [2, 11].

Based on these models, several techniques attempt to reconstruct pathways. Deterministic tractography involves directly following the diffusion pathways. In the single tensor model, this means simply following the principal diffusion direction [6], while multi-fiber models often include techniques for determining the number of fibers present or when pathways branch [16, 17, 25]. Kalman and particle filters have been used with single tensor streamline tractography [8, 15, 49], but these are used for path regularization and not to estimate the underlying fiber model. Another approach to regularizing single tensor tractography uses a moving least squares estimate weighted

with the previous tensor [50]. In this present study we focus on deterministic techniques, but probabilistic methods have also been developed to form connections by sampling [7, 19, 34].

Several studies have specific relevance to this present work because of their use of a filtering strategy in either orientation estimation or tractography. In extending standard streamline tractography to enhance path regularization, [15] move curve integration into a linear Kalman filter while [50] incorporate a moving least squares estimator. Alternatively, one could use a particle filter to place a prior on the direction of propagation [49]. Since these methods model only the position of the fiber, not the local fiber model, they are inherently focused on path regularization rather than estimating the underlying fiber structure. Finally, [38] proposed using a linear Kalman filter for online, direct estimation of either single-tensor or harmonic coefficients while successive diffusion image slices are acquired, while [9] revisited the technique to account for proper regularization and proposed a method to quickly determine optimal gradient set orderings.

1.2 *Filtered Tractography*

Of the approaches listed above, nearly all fit the model at each voxel independent of other voxels; however, tractography is a causal process: we arrive at each new position along the fiber based upon the diffusion found at the previous position.

We propose to we treat model estimation and tractography as such by placing this process within a causal filter. As we examine the signal at each new position, the filter recursively updates the underlying local model parameters, provides the variance of that estimate, and indicates the direction in which to propagate tractography. Figure 2 provides an overview of this recursive process.

To begin estimating within a finite dimensional filter, we model the diffusion signal

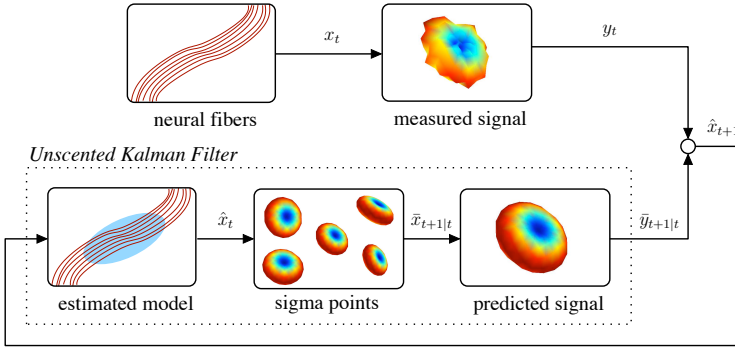


Figure 2: System overview illustrating relation between the neural fibers, the measured scanner signal, and the unscented Kalman filter as it is used to estimate the local model. At each step, the filter uses its current model state ($\hat{\mathbf{x}}_t$) to predict the observed scanner signal ($\bar{\mathbf{y}}_{t+1|t}$) and then compares that against the actual measured signal (\mathbf{y}_t) in order to update its internal model state ($\hat{\mathbf{x}}_{t+1}$).

using a mixture of Watson functions. We choose the Watson function since it provides a compact representation of the signal parameterized by the principal diffusion direction and a scaling parameter describing anisotropy, and further allows analytic reconstruction of the oriented diffusion function from those parameters [40]. This enables estimation directly from the raw signal without separate preprocessing or regularization. Because the signal reconstruction is nonlinear, we use the unscented Kalman filter to estimate the model parameters and then propagate in the most consistent direction. Using causal estimation in this way yields inherent path regularization and accurate fiber resolution at crossing angles not found with independent optimization. In a loop, the filter estimates the model at the current position, moves a step in the most consistent direction, and then begins estimation again. Since each iteration begins with a near-optimal solution provided by the previous estimation, the convergence of model fitting is improved and many local minima are naturally avoided. This approach generalizes to arbitrary fiber model with finite dimensional parameter space.

Section 1.2.1 provides the necessary background on modeling the measurement signal using directional functions and defines the specific fiber model employed in

this proposal. Then, Section 1.2.2 describes how this model may be estimated using an unscented Kalman filter.

1.2.1 Modeling local fiber orientations

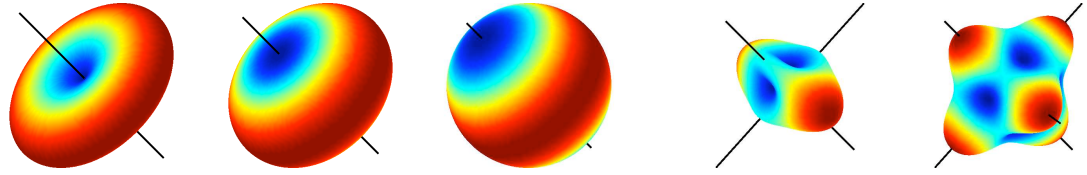
In diffusion weighted imaging, image contrast is related to the strength of water diffusion, and our goal is to accurately relate these signals to an underlying model of fiber orientation. At each image voxel, diffusion is measured along a set of distinct gradients, $\mathbf{u}_1, \dots, \mathbf{u}_n \in \mathbb{S}^2$ (on the unit sphere), producing the corresponding signal, $\mathbf{s} = [s_1, \dots, s_n]^T \in \mathbb{R}^n$. For voxels containing a mixed diffusion pattern, a general weighted formulation may be written as,

$$s_i = s_0 \sum_j w_j e^{-b\mathbf{u}_i^T D_j \mathbf{u}_i}, \quad (1)$$

where s_0 is a baseline signal intensity, b is an acquisition-specific constant, w_j are convex weights, and D_j is a tensor matrix describing a diffusion pattern.

Considering a single tensor, we now follow the formulation of Rathi et al. [40] to define the Watson directional function which approximates the apparent diffusion pattern. We begin by noting that any diffusion tensor D can be decomposed as $D = U\Lambda U^T$, where U is a rotation matrix and Λ is a diagonal matrix with eigenvalues $\{\lambda_1, \lambda_2, \lambda_3\}$. These eigenvalues determine the shape of the tensor: ellipsoidal, planar, and spherical. For example, if $\lambda_1 > \lambda_2 > \lambda_3$, then the shape is ellipsoidal with the major axis of the ellipsoid pointing to the eigenvector corresponding to λ_1 . Intuitively, it represents strong diffusion along that particular direction. When $\lambda_1 = \lambda_2 > \lambda_3$, the shape is planar indicating diffusion along orthogonal directions, and finally, when $\lambda_1 = \lambda_2 = \lambda_3$, the diffusion is spherical (isotropic).

The most common of these configurations is ellipsoidal with principal diffusion direction \mathbf{m} and eigenvalue λ_1 , and hence the first step in introducing directional functions is to approximate the tensor by its first eigenvector expansion: $D \approx \lambda_1 \mathbf{m} \mathbf{m}^T$.



(a) Reconstructed signals for strong diffusivity ($k = 2$), weak diffusivity ($k = 0.5$), and isotropic diffusion patterns ($k = 0.01$).
(b) Signals for two-fiber and three-fiber mixtures.

Figure 3: Watson directional functions are capable of representing various diffusion patterns and fiber orientations.

Using this, each exponent in Equation 1 may then be rewritten,

$$-b\mathbf{u}_i^T D \mathbf{u}_i \approx -b\lambda_1 \mathbf{u}_i^T (\mathbf{m}\mathbf{m}^T) \mathbf{u}_i \quad (2)$$

$$= -b\lambda_1 (\mathbf{u}_i^T \mathbf{m})^2 \quad (3)$$

$$= -k (\mathbf{u}_i^T \mathbf{m})^2, \quad (4)$$

where the scalar k concentration parameter determines the degree of anisotropy. Finally, the general model may be restated:

$$s_i = A \sum_j w_j e^{-k_j (\mathbf{u}_i^T \mathbf{m}_j)^2}, \quad (5)$$

where A is a normalization constant such that $\|\mathbf{s}\| = 1$. For purposes of comparison, this normalization will also be done to signals obtained from scanner. Note that, while the diffusion tensor requires six parameters, these Watson functions require four parameters: three for the orientation vector \mathbf{m} and one concentration parameter k . Employing a spherical representation can further reduce the unit vector \mathbf{m} to two spherical coordinates. Figure 3a demonstrates how adjusting the k -value produces different diffusion patterns, and Figure 3b illustrates two multi-fiber configurations.

From this general mixture model, we choose to start with a restricted form involving two equally-weighted Watson functions. This choice is guided by several previous studies. Behrens et al. [7] showed that at a b -value of 1000 ms/mm^2 the maximum number of detectable fibers is two. Several other studies have also found

two-fiber models to be sufficient [25, 36, 46, 48]. Using this as a practical guideline, we started with a mixture of two Watson functions as our local fiber model. Further, following the study of [48], we assume an equal combination (50%-50%) of the two Watson functions. While the effect of this second choice appears to have little to no effect on experiments, we have yet to quantify any potential loss in accuracy. These assumptions leave us with the following two-fiber model used in this study:

$$s_i = \frac{A}{2} \left(e^{-k_1(\mathbf{u}_i^T \mathbf{m}_1)^2} + e^{-k_2(\mathbf{u}_i^T \mathbf{m}_2)^2} \right). \quad (6)$$

where k_1 and \mathbf{m}_1 parameterize the first Watson function, k_2 and \mathbf{m}_2 parameterize the second, and A is again a normalization constant such that $\|\mathbf{s}\| = 1$. Thus, the equally-weighted two-fiber model is fully described by the following parameters: k_1 , \mathbf{m}_1 , k_2 , \mathbf{m}_2 .

Finally, from such parameters, Rathi et al. [40] describe how one may compute the ODF analytically by applying the Funk-Radon transform directly to Equation 5. The ODF can be reconstructed directly from the same parameters describing the signal without a separate estimation process. For the two-Watson model (Equation 6) the ODF is approximated by,

$$f_i = \frac{B}{2} \left(e^{-\frac{k_1}{2}(1-(\mathbf{u}_i^T \mathbf{m}_1)^2)} + e^{-\frac{k_2}{2}(1-(\mathbf{u}_i^T \mathbf{m}_2)^2)} \right), \quad (7)$$

where B is a normalization factor such that $\sum_i f_i = 1$.

1.2.2 Estimating the fiber model

Given the measured scanner signal at a particular voxel, we want to estimate the underlying model parameters that explain this signal. As in streamline tractography, we treat the fiber as the trajectory of a particle which we trace out. At each step, we examine the measured signal at that position, estimate the underlying model parameters, and propagate forward in the most consistent direction. Figure 2 illustrates this filtering process.

To use a state-space filter for estimating the model parameters, we need the application-specific definition of four filter components:

1. The system state \mathbf{x} : the model parameters
2. The state transition $f[\cdot]$: how the model changes as we trace the fiber
3. The observation $h[\cdot]$: how the signal appears given a particular state
4. The measurement \mathbf{y} : the actual signal obtained from the scanner

For our state, we directly use the model parameters, thus the two-fiber model in Equation 6 has the following state vector:

$$\mathbf{x} = [\mathbf{m}_1 \ k_1 \ \mathbf{m}_2 \ k_2]^T, \quad \mathbf{m} \in \mathbb{S}^2, k \in \mathbb{R}. \quad (8)$$

While each \mathbf{m} could be represented in a reduced spherical form, the antipodes of the spherical parameterization would then introduce nonlinearities which complicate estimation. For the state transition we assume identity dynamics; the local fiber configuration does not undergo drastic change from one position to the next. Our observation is the signal reconstruction, $\mathbf{y} = \mathbf{s} = [s_1, \dots, s_n]^T$ using s_i from Equation 6, and our measurement is the actual signal interpolated directly from the diffusion weighted images at the current position.

Since the signal reconstruction is a nonlinear process, we employ an unscented Kalman filter to perform nonlinear estimation. Similar to classical linear Kalman filtering, the unscented version seeks to reconcile the predicted state of the system with the measured state and addresses the fact that those two processes (prediction and measurement) may be nonlinear or unknown. It does this in two phases: first it uses the system transition model to predict the next state and observation, and then it uses the new measurement to correct that state estimate. In what follows, we present the algorithmic application of the filter. For more thorough treatments, see [22, 47].

It is important to note two alternative techniques for nonlinear estimation. First, particle filters are commonly used to provide a multi-modal estimate of unknown systems. With respect to an n -dimensional state space, particle filters require the number of particles to be exponential to properly explore the state space. In contrast, the unscented filter requires only $2n + 1$ particles (sigma points) for a Gaussian estimate that space. Further, for many slowly varying systems, the multi-modal estimate is unnecessary: from one voxel to the next, fibers tend not to change direction drastically. Second, an extended Kalman filter may also be used to provide a Gaussian estimate after linearizing the system; however, the unscented Kalman filter provides a more accurate estimate with equivalent computational cost and altogether avoids the attempt at linearization [22, 27, 47].

Suppose the system of interest is at time t and we have a Gaussian estimate of its current state with mean, $\mathbf{x}_t \in \mathbb{R}^n$, and covariance, $P_t \in \mathbb{R}^{n \times n}$. Prediction begins with the formation of a set $\mathbf{X}_t = \{\mathbf{x}_i\} \subset \mathbb{R}^n$ of $2n + 1$ *sigma point* states with associated convex weights, $w_i \in \mathbb{R}$, each a perturbed version of the current state. We use the covariance, P_t , to distribute this set:

$$\begin{aligned} \mathbf{x}_0 &= \mathbf{x}_t & w_0 &= \kappa/(n + \kappa) & w_i &= w_{i+n} = \frac{1}{2(n+\kappa)} \\ \mathbf{x}_i &= \mathbf{x}_t + \left[\sqrt{(n + \kappa)P_t} \right]_i & \mathbf{x}_{i+n} &= \mathbf{x}_t - \left[\sqrt{(n + \kappa)P_t} \right]_i \end{aligned} \quad (9)$$

where $[A]_i$ denotes the i^{th} column of matrix A and κ is an adjustable scaling parameter ($\kappa = 0.01$ in all experiments). Next, this set is propagated through the state transition function, $\hat{\mathbf{x}} = f[\mathbf{x}] \in \mathbb{R}^n$, to obtain a new predicted sigma point set: $\mathbf{X}_{t+1|t} = \{f[\mathbf{x}_i]\} = \{\hat{\mathbf{x}}_i\}$. Since in this study we assume the fiber configuration does not change drastically as we follow it from one voxel to the next, we may write this identity transition as, $\mathbf{x}_{t+1|t} = f[\mathbf{x}_t] = \mathbf{x}_t$. These are then used to calculate the predicted system mean state and covariance,

$$\bar{\mathbf{x}}_{t+1|t} = \sum_i w_i \hat{\mathbf{x}}_i,$$

$$P_{xx} = \sum_i w_i (\hat{\mathbf{x}}_i - \bar{\mathbf{x}}_{t+1|t}) (\hat{\mathbf{x}}_i - \bar{\mathbf{x}}_{t+1|t})^T + Q, \quad (10)$$

where Q is the injected process noise bias used to ensure a non-null spread of sigma points and a positive-definite covariance. This procedure comprises the *unscented transform* used to estimate the behavior of a nonlinear function: spread sigma points based on your current uncertainty, propagate those using your transform function, and measure their spread.

To obtain the predicted observation, we again apply the unscented transform this time using the predicted states, $\mathbf{X}_{t+1|t}$, to estimate what we expect to observe from the hypothetical measurement of each state: $\mathbf{y} = h[\hat{\mathbf{x}}] \in \mathbb{R}^m$. Keep in mind that, for this study, our observation is the signal reconstruction from Equation 6, and the measurement itself is the diffusion-weighted signal, \mathbf{s} , interpolated at the current position. From these, we obtain the predicted set of observations, $\mathbf{Y}_{t+1|t} = \{h[\hat{\mathbf{x}}_i]\} = \{\mathbf{y}_i\}$, and may calculate its weighted mean and covariance,

$$\begin{aligned} \bar{\mathbf{y}}_{t+1|t} &= \sum_i w_i \hat{\mathbf{y}}_i, \\ P_{yy} &= \sum_i w_i (\hat{\mathbf{y}}_i - \bar{\mathbf{y}}_{t+1|t}) (\hat{\mathbf{y}}_i - \bar{\mathbf{y}}_{t+1|t})^T + R, \end{aligned} \quad (11)$$

where R is the injected measurement noise bias again used to ensure a positive-definite covariance. The cross correlation between the estimated state and measurement may also be calculated:

$$P_{xy} = \sum_i w_i (\hat{\mathbf{x}}_i - \bar{\mathbf{x}}_{t+1|t}) (\hat{\mathbf{y}}_i - \bar{\mathbf{y}}_{t+1|t})^T. \quad (12)$$

As is done in the classic linear Kalman filter, the final step is to use the Kalman gain, $K = P_{xy}P_{yy}^{-1}$, to correct our prediction and provide us with the final estimated system mean and covariance,

$$\mathbf{x}_{t+1} = \bar{\mathbf{x}}_{t+1|t} + K(\mathbf{y}_t - \bar{\mathbf{y}}_{t+1|t}) \quad (13)$$

$$P_{t+1} = P_{xx} - KP_{yy}K^T, \quad (14)$$

Algorithm 1 Unscented Kalman Filter

- 1: Form weighted sigma points $\mathbf{X}_t = \{w_i, \mathbf{x}_i\}_{i=0}^{2n}$ around current mean \mathbf{x}_t and covariance P_t with scaling factor ζ

$$\mathbf{x}_0 = \mathbf{x}_t \quad \mathbf{x}_i = \mathbf{x}_t + [\sqrt{\zeta P_t}]_i \quad \mathbf{x}_{i+n} = \mathbf{x}_t - [\sqrt{\zeta P_t}]_i$$

- 2: Predict the new sigma points and observations

$$\mathbf{X}_{t+1|t} = f[\mathbf{X}_t] \quad \mathbf{Y}_{t+1|t} = h[\mathbf{X}_{t+1|t}]$$

- 3: Compute weighted means and covariances, *e.g.*

$$\bar{\mathbf{x}}_{t+1|t} = \sum_i w_i \mathbf{x}_i \quad P_{xy} = \sum_i w_i (\mathbf{x}_i - \bar{\mathbf{x}}_{t+1|t})(\mathbf{y}_i - \bar{\mathbf{y}}_{t+1|t})^T$$

- 4: Update estimate using Kalman gain K and scanner measurement \mathbf{y}_t

$$K = P_{xy} P_{yy}^{-1} \quad \mathbf{x}_{t+1} = \bar{\mathbf{x}}_{t+1|t} + K(\mathbf{y}_t - \bar{\mathbf{y}}_{t+1|t}) \quad P_{t+1} = P_{xx} - K P_{yy} K^T$$

where $\mathbf{y}_t \in \mathbb{R}^m$ is the actual signal measurement taken at this time. Algorithm 1 summarizes this algorithm for unscented Kalman filtering.

1.2.3 The algorithm

To summarize the proposed technique, we are using the unscented Kalman filter to estimate the local model parameters as we trace out each fiber. For each fiber, we maintain the position at which we are currently tracing it and the current estimate of its model parameters (mean and covariance). At each iteration of the algorithm, we predict the new state, which in this case is simply identity: $\mathbf{x}_{t+1|t} = \mathbf{x}_t$. Our actual measurement \mathbf{y}_t in Equation 13 is the diffusion-weighted signal, \mathbf{s} , recorded by the scanner at this position. At subvoxel positions we interpolate directly on the diffusion-weighted images. With these, we step through the equations above to find the new estimated model parameters, \mathbf{x}_{t+1} . Last, we use second-order Runge-Kutta integration to move a small step in the most consistent of principal diffusion directions, and then we repeat these steps from that new location. Algorithm 2 outlines the integration of filtering and tractography.

Algorithm 2 Main loop repeated for each fiber

- 1: **repeat**
 - 2: Form the sigma points \mathbf{X}_t around \mathbf{x}_t
 - 3: Predict the new sigma points $\mathbf{X}_{t+1|t}$ and observations $\mathbf{Y}_{t+1|t}$
 - 4: Compute weighted means and covariances, *e.g.* $\bar{\mathbf{x}}_{t+1|t}$, P_{xy}
 - 5: Update estimate $(\mathbf{x}_{t+1}, P_{t+1})$ using scanner measurement (\mathbf{y}_t)
 - 6: Proceed in most consistent direction \mathbf{m}_j
 - 7: **until** estimated model appears isotropic
-

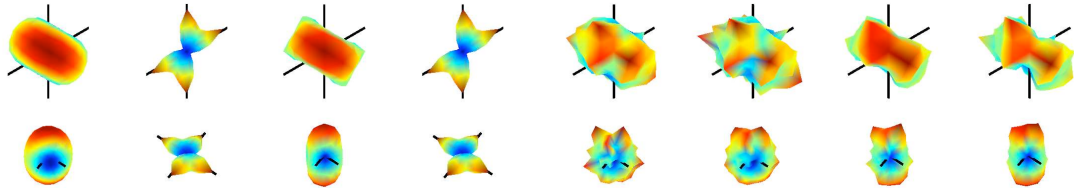
CHAPTER II

PRELIMINARY RESULTS

We first use experiments with synthetic data to validate our technique against ground truth. We confirm that our approach accurately estimates the true underlying signal and reliably recognizes crossing fibers over a broad range of angles. Comparing against two alternative multi-fiber optimization techniques, we find the filtered approach gives consistently superior results in both respects (Section 2.1). Next, we perform tractography through crossing fiber fields and examine the underlying orientations and branchings (Section 2.2). Lastly, we examine a real dataset to demonstrate how causal estimation is able to pick up fibers and branchings known to exist *in vivo* yet absent using other techniques (Section 2.3).

Following the experimental method of generating synthetic data found in [12, 42, 44], we pull from our real data set the 300 voxels with highest fractional anisotropy (FA) and compute the average eigenvalues among these voxels: $\{1200, 100, 100\} \mu\text{m}^2/\text{msec}$ ($\text{FA}=0.91$). We generated synthetic MR signals according to Equation 1 using these eigenvalues to form an anisotropic tensor at both $b = 1000$ and $b = 3000$, using 81 gradient directions uniformly spread on the hemisphere, and assume $s_0 = 1$. We generate two separate data sets, each with a different level of Rician noise: low-noise ($\sigma = 0.1$, $\text{SNR} \approx 10 \text{ dB}$) and high-noise ($\sigma = 0.2$, $\text{SNR} \approx 5 \text{ dB}$). To get an idea of this level of noise, Figure 4 visualizes a sample voxel with two fibers at a 60° angle.

Throughout the experiments, we draw comparison to three alternative techniques. First, we use the same two-Watson model from Section 1.2.1 with a variant of matching pursuit for brute force, dictionary-based optimization [30]. In our implementation, we construct a finite dictionary of two-Watson signals at a range of various k -values,



(a) Ground truth signal and ODF ($b=1000$, $b=3000$).
(b) Low- and high-noise signals ($b=1000$, $b=3000$).

Figure 4: Synthetic two-fiber voxel signals at a 60° angle (*black wires indicate principal diffusion directions*). Each column shows the same surface from two viewpoints. (a) shows the ground truth signal and corresponding true ODF (*left to right*). (b) shows the corrupted versions of the ground truth signal (*left to right*).

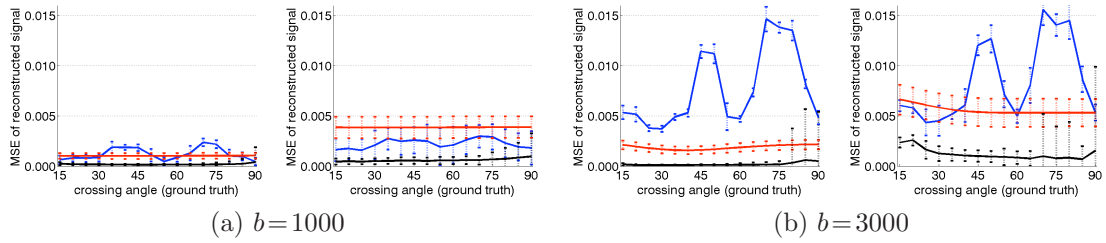


Figure 5: Mean squared error (MSE) between reconstructed signal and ground truth signal at various crossing angles (*low-noise on left, high-noise on right*). Notice how the increased noise has little effect on the filter (*black*) compared to using matching pursuit (*blue*) or sharpened spherical harmonics (*red*).

essentially discretizing the search space across orientations and k -values. Given a new measured signal, the signal from the dictionary with highest inner product provides an estimate of orientation and concentration. While our signal is produced at 81 gradient directions, we use 341 directions to construct the dictionary, thus any error is due to the method's sensitivity to noise and discretization. Note that by using 341 orientation directions there is roughly an 8° angular difference between offset orientations, hence we see that the angular error is often at most 8° . This approach highlights the effect of using the same model but changing the optimization technique to one that treats each voxel independently. Second, we use spherical harmonics for modeling [44] and fiber-ODF sharpening for peak detection as described in [12] (order $l=8$, regularization $L=0.006$). This provides a comparison with an

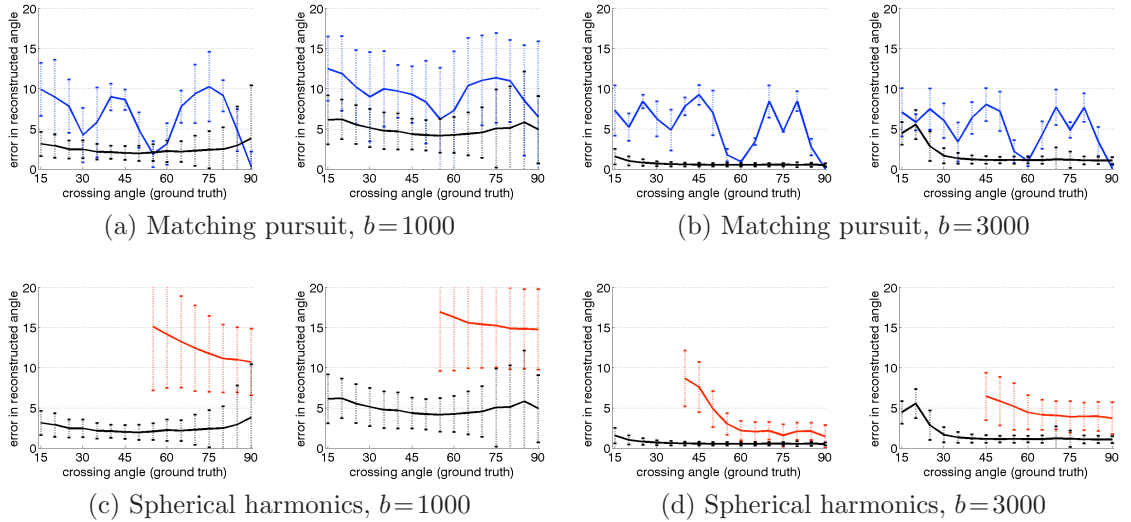


Figure 6: Average angle error at various crossing angles comparing all three techniques: matching pursuit (*blue*), sharpened spherical harmonics (*red*), and the proposed filter (*black*). The filter provides stable and consistent estimation compared to either alternative technique. Each subfigure shows both the low-noise and high-noise experiments (*left, right*).

independently estimated, model-free representation. Note that this technique is very similar to spherical deconvolution. Last, when performing tractography on real data, we use single-tensor streamline tractography as a baseline¹.

The unscented Kalman filter conveniently requires few parameters. Specifically, of importance are the matrices for injecting model noise Q and injecting measurement noise R (see Equation 10 and Equation 11). Fortunately, the relative magnitude of each can be determined off-line from the data itself. We found that values on the order of $q_m = 0.001$ (roughly 2°), $q_\lambda = 10$, and $r_s = 0.02$ were quite robust for the appropriate diagonal entries of Q and R . Off-diagonal entries were left at zero.

2.1 Signal reconstruction and angular resolution

While the independent optimization techniques can be run on individually generated voxels, care must be taken in constructing reasonable scenarios to test the causal

¹Using the freely available Slicer 2.7 (<http://www.slicer.org>).

filter. For this purpose, we constructed an actual 2D field through which to navigate (see Figure 7 and Figure 8a). In the middle is one long fiber pathway where the filter begins estimating a single component but then runs into a field of voxels with two crossed fibers at a fixed angle. In this crossing region we calculated error statistics. Similarly, we computed the angular error over this region using both sharpened spherical harmonics and matching pursuit. We generated several similar fields, each at a different fixed angle. By varying the size of the crossing region or the number of fibers run, we ensured that each technique performed estimation on at least 500 voxels.

In the first experiment, we look at signal reconstruction error. We calculate the mean squared error of the reconstructed signal, \mathbf{s} , against the ground truth signal, $\hat{\mathbf{s}}$ (pure, no noise): $\|\mathbf{s} - \hat{\mathbf{s}}\|^2 / \|\hat{\mathbf{s}}\|^2$. In essence, this is exactly what the filter is trying to minimize: the error between the reconstructed signal and the measured signal. Figure 5 shows the results of using the proposed filter, matching pursuit, and spherical harmonics. Over each technique's series of estimations, the trendlines indicate the mean error while the bars indicate one standard deviation. Spherical harmonics (*red*) appear to produce a smooth fit to the given noisy data, while matching pursuit (*blue*) shows the effect of discretization and sensitivity to noise. The two raised areas are a result of the dictionary being constructed with an 8° minimum separation between any pair of orientations. This experiment demonstrates that the proposed filter (*black*) accurately and reliably estimates the true underlying signal.

In the second experiment, we looked at the error in angular resolution by comparing the filtered approach to matching pursuit and sharpened spherical harmonics. Figure 6a and Figure 6b show the sensitivity of matching pursuit. Consistent with the results reported in [10,12], spherical harmonics are generally unable to detect and resolve angles below 50° for $b = 1000$ or below 40° for $b = 3000$. Figure 6c and Figure 6d confirm this, respectively. This experiment demonstrates that for $b=1000$, the

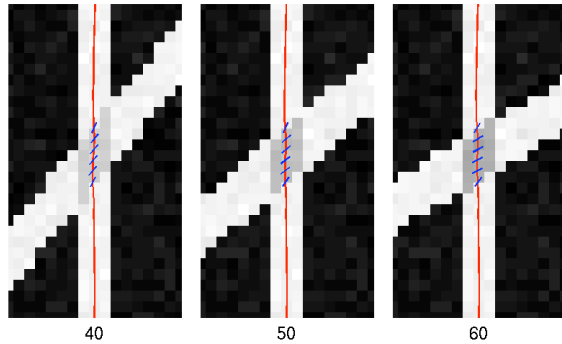
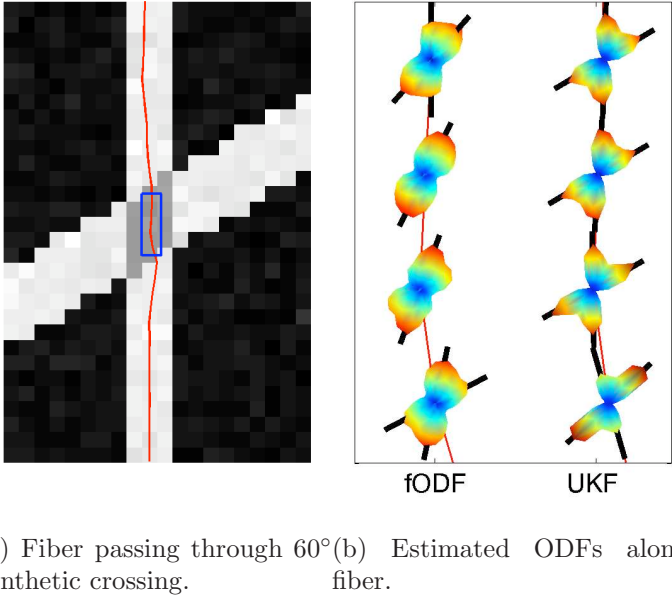


Figure 7: Fiber passing through 40° , 50° , and 60° synthetic crossings ($b=3000$, noisy). Blue dashes represent the orientation of the second fiber when detected.

filtered approach consistently resolves angles down to $20\text{-}30^\circ$ with 5° error compared to independent optimization which fails to reliably resolve below 60° with as much as 15° error. For $b=3000$, the filtered approach consistently resolves down to $20\text{-}30^\circ$ with $2\text{-}3^\circ$ error compared to independent optimization which cannot resolve below 50° with 5° error.

2.2 Synthetic tractography

Having verified the technique’s accuracy, we now turn to the resulting tractography. Figure 7 provides examples of synthetic crossing fiber fields each at different fixed angles: 40° , 50° , 60° ($b=3000$, noisy). In our experiments, we start fibers from the bottom and propagate upward where they encounter the crossing region. Here we show one such fiber and use blue glyphs to indicate the second component detected as it passes through the crossing region. In general, we found that in regions with only one true fiber present (those outside the crossing), the second component either aligned with the first or adjusted its concentration parameter to fill out the isotropic component of the signal. Further, we found the filtering strategy to be robust with respect to initial configuration and choice of injected noise matrices Q and R (Equation 10 and Equation 11).



(a) Fiber passing through 60°(b) Estimated ODFs along
synthetic crossing. fiber.

Figure 8: One fiber passing through an example synthetic field ($b=1000$, noisy) and the estimated ODFs using spherical harmonics and the filter as it passes through the crossing region (blue box). The filter provides consistent angular resolution along the fiber while independent spherical harmonic modeling at those same locations misses the second fiber in two voxels.

In Figure 8a we show another 60° field ($b=1000$, noisy) but take a closer look at several points along a single fiber as it passes through the crossing region. We also examine the corresponding ODFs reconstructed using sharpened spherical harmonics and the proposed filter. As expected, the sharpened spherical harmonics often do not detect the crossing but result in a single angle as seen in the middle two samples in Figure 8b. A close examination of the reported axes shows the bias toward a single averaged axis as reported in [42, 43, 48]. In contrast, the filtered results are consistent and accurate.

2.3 *In vivo tractography*

We tested our approach on a real human brain scan acquired on a 3-Tesla GE system using an echo planar imaging (EPI) diffusion weighted image sequence. A double echo option was used to reduce eddy-current related distortions. To reduce impact of EPI

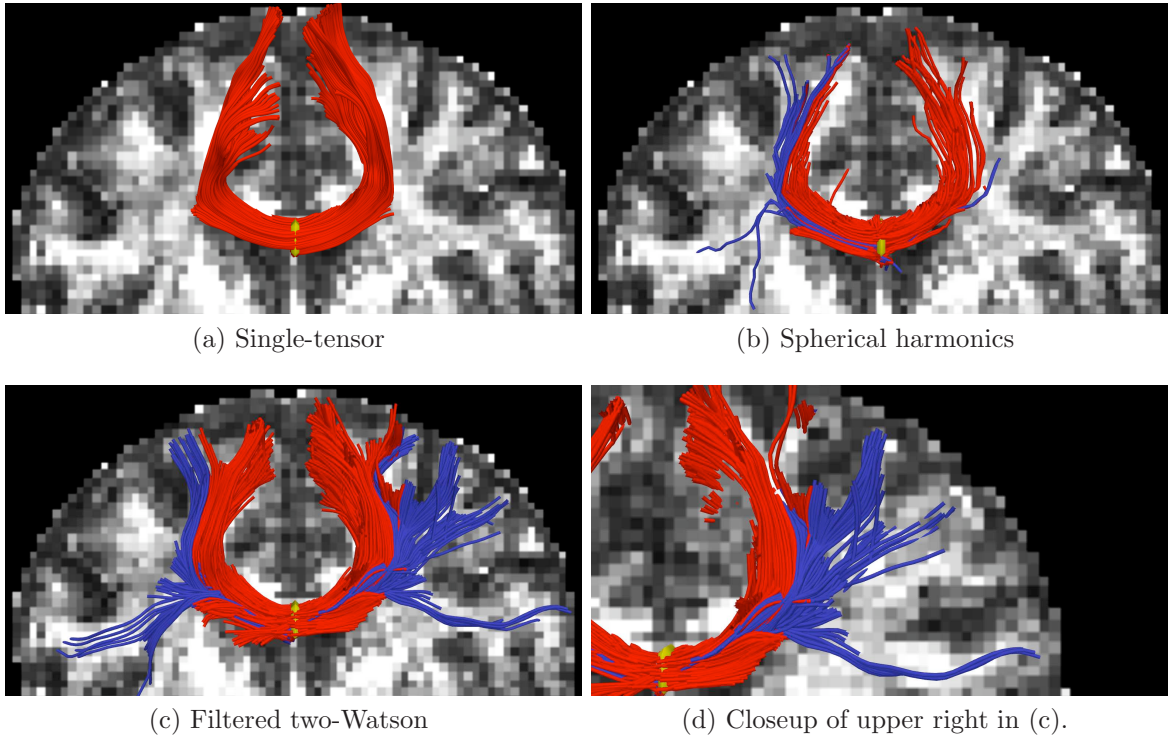


Figure 9: Filtered tractography picks up many fiber paths consistent with the underlying structures. Both single-tensor streamline and sharpened spherical harmonics are unable to find the majority of these pathways. Fibers existing ± 22 mm around the mid-sagittal plane are indicated in blue. Seed region indicated in yellow.

spatial distortion, an eight channel coil was used to perform parallel imaging using Array Spatial Sensitivity Encoding Techniques (GE) with a SENSE-factor (speed-up) of 2. Acquisitions have 51 gradient directions with $b = 900$ and eight baseline scans with $b=0$. The original GE sequence was modified to increase spatial resolution, and to further minimize image artifacts. The following scan parameters were used: TR 17000 ms, TE 78 ms, FOV 24 cm, 144x144 encoding steps, 1.7 mm slice thickness. All scans had 85 axial slices parallel to the AC-PC line covering the whole brain. In addition, $b=0$ field inhomogeneity maps were collected and calculated.

We first focused on fibers originating in the corpus callosum. Specifically, we sought to trace out the lateral transcallosal fibers that run through the corpus callosum out to the lateral gyri. It is known that single-tensor streamline tractography only

traces out the dominant pathways forming the U-shaped callosal radiation (Figure 9a and Figure 10a). Several studies document this phenomena, among them the works of Descoteaux et al. [12] and Schultz and Seidel [42] have side-by-side comparisons. These fibers have been reported in using diffusion spectrum imaging [17], probabilistic tractography [5, 12, 23], and more recently with tensor decomposition [42].

We start with two basic experiments: first examining the tracts surrounding a single coronal slice and second looking at all tracts passing through the corpus callosum. We seed each algorithm multiple times in voxels at the intersection of the mid-sagittal plane and the corpus callosum. To explore branchings found using the proposed technique, we considered a component to be branching if it was separated from the primary component by less than 40° with $k \geq 0.6$. Similarly, with sharpened spherical harmonics, we considered it a branch if we found additional maxima over the same range. We terminated fibers when the general fractional anisotropy of the estimated signal (std/rms) fell below 0.1. While such heuristics are somewhat arbitrary, we found little qualitative difference in adjusting these values.

For the first experiment, Figure 9 shows tracts originating from within a few voxels intersecting a particular coronal slice. For a reference backdrop, we use a coronal slice showing the intensity of fractional anisotropy (FA) placed a few voxels behind the seeded coronal position. Keeping in mind that these fibers are intersecting or are in front of the image plane, this roughly shows how the fibers navigate the areas of high anisotropy (bright regions). Similar to the results in [12, 42], Figure 9b shows that sharpened spherical harmonics only pick up a few fibers intersecting the U-shaped callosal radiata. In contrast, our proposed method traces out many pathways consistent with the apparent anatomy. To emphasize transcallosal tracts, we color as blue those fibers exiting a corridor of ± 22 mm around the mid-sagittal plane. Figure 9d provides a closer inspection of Figure 9c where, to emphasize the underlying anatomy influencing the fibers, we use as a backdrop the actual coronal slice passing

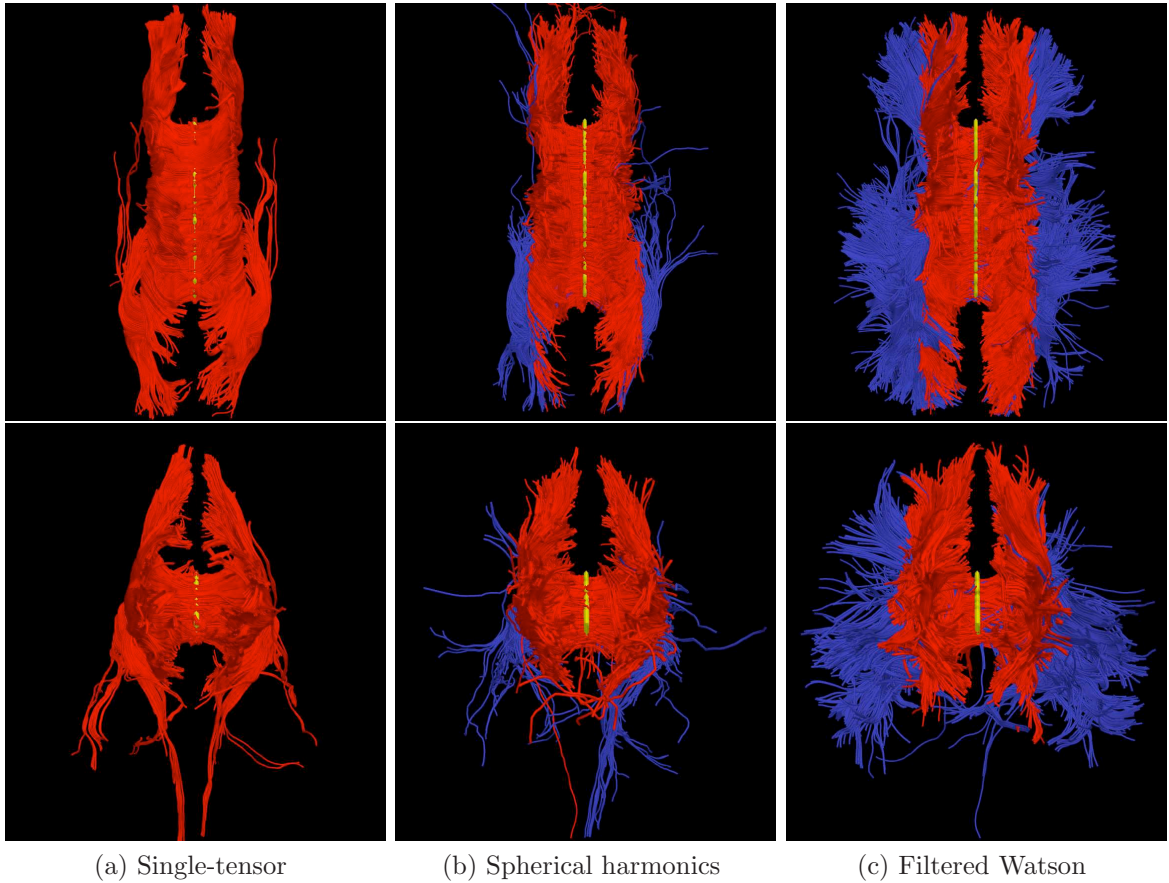


Figure 10: Tracing fibers originating from the center of the entire corpus callosum with views from above (*top rows*) and front-to-back (*bottom rows*). The proposed filtered tractography is able to find many of the lateral projections (*blue*) while single-tensor is unable to find any and few are found with sharpened spherical harmonics. Seed region indicated in yellow.

through the voxels used to seed this run. Such results are obtained in minutes in our current MATLAB implementation. At each step, the cost of reconstructing the signal for few sigma points approaches the cost of a few iterations of weighted least-squares estimation of a single tensor.

For the second experiment, Figure 10 shows a view of the whole brain to see the overall difference between the different methods. Here again we emphasize with blue the transcallosal fibers found using the proposed filter. To show the various pathways infiltrating the gyri, Figure 11 provides a closeup of the frontal lobe from above (without blue emphasis).

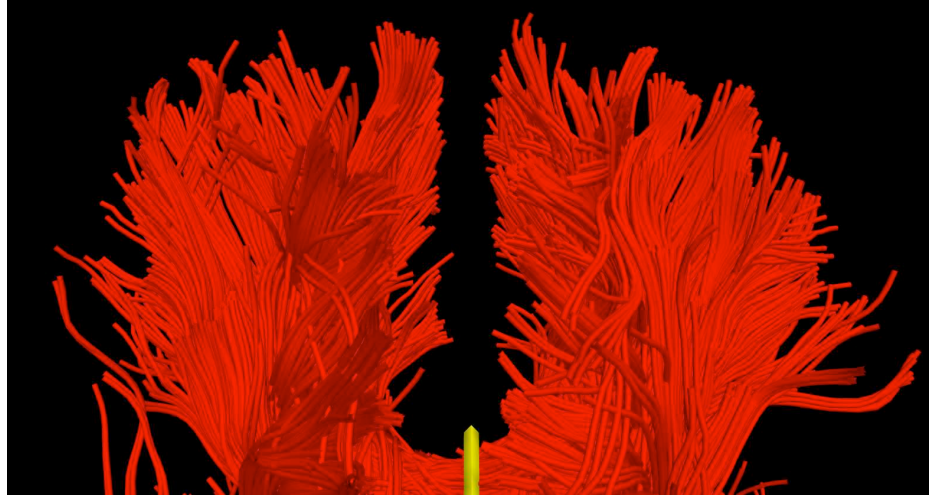


Figure 11: Closeup of frontal fibers in Figure 10c viewed from above.

Next we examined fibers passing through the internal capsule to trace out the pathways reaching up into the primary motor cortex at the top of the brain as well as down into the hippocampal regions near the brain stem. Figure 12 shows frontal views for each technique with seeding near the cerebral peduncles (*yellow*). Figure 14 shows this same result from a side view where we can see that the filtered approach picks up the corticospinal pathways. As reported elsewhere [7], single-tensor tractography follows the dominant corticospinal tract to the primary motor cortex. The same pathways were also found with spherical harmonics. Figure 13 shows a view from above where we use a transverse FA image slice near the top of the brain as a backdrop so we can focus on the fiber endpoints. From this we can see how each method infiltrates the sulci grooves, and specifically we see that the filtered method is able to infiltrate sulci more lateral compared to single-tensor tractography.

Note that in the region of intersection between the transcallosal fibers, the corticospinal, and the superior longitudinal fasciculus, the partial voluming of each of these pathways leads the filter to report several end-to-end connections that are not necessarily present, *e.g.* fibers originating in the left internal capsule do not pass through this region, through the corpus callosum and then insert into the right motor

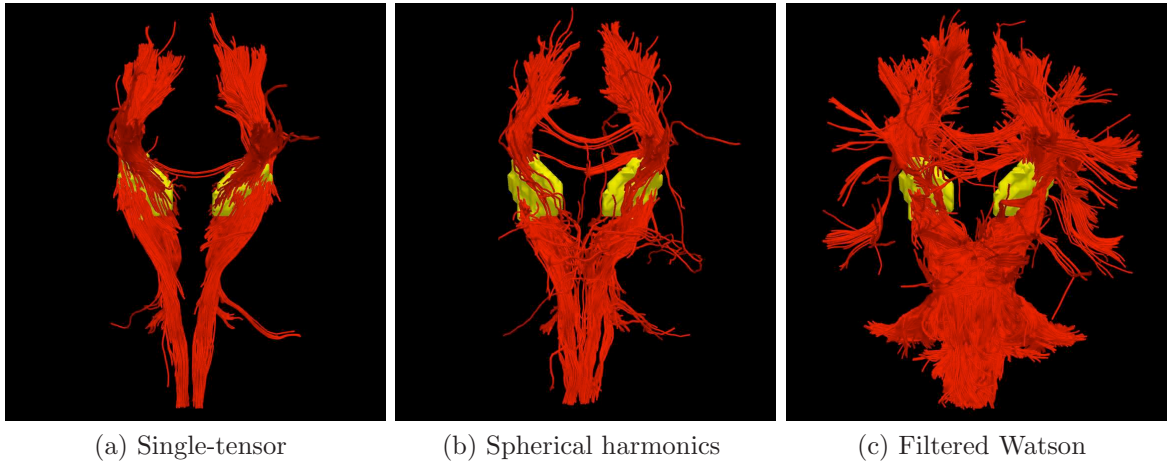


Figure 12: Frontal view with seeding in the internal capsule (*yellow*). While both single-tensor and spherical harmonics tend to follow the dominant corticospinal tract to the primary motor cortex, the filtered approach follows many more pathways. Seed region indicated in yellow.

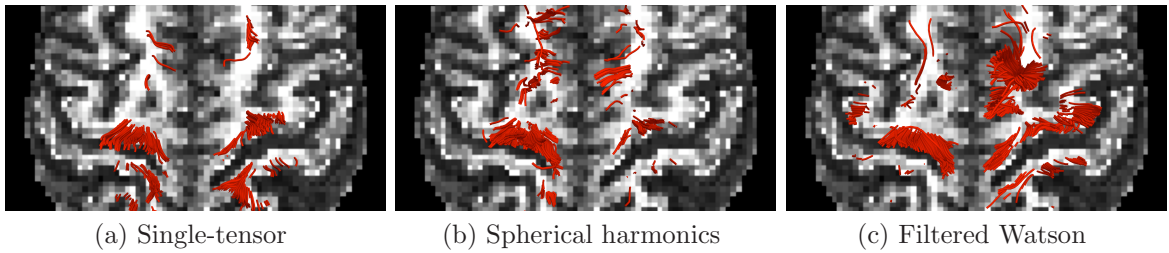


Figure 13: View from above showing cortical insertion points for each method. FA backdrop is taken near the top of the brain. The filtered approach shows more lateral insertions compared to single-tensor and spherical harmonic tracts.

cortex. Many of the lateral extensions are callosal fibers that are picked up while passing through this juncture. It is our hope that such connections may be avoided with the introduction of weighted mixtures, alternative filter formulations, or different heuristic choices in the algorithm.

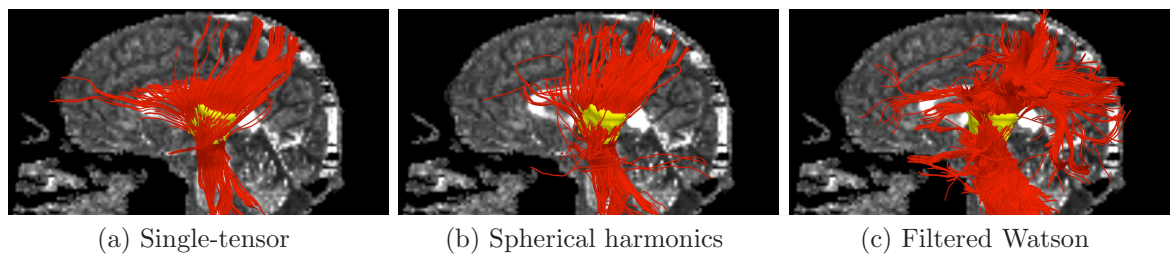


Figure 14: Side view with seeding in the internal capsule (*yellow*). Filtered tractography finds many insertions into cortical regions of the parietal and occipital lobes. Seed region indicated in yellow.

CHAPTER III

PROPOSED RESEARCH

The goal of this thesis is to develop an accurate and reliable method of tracing neural pathways. This entails development of the technique itself and comparison against relevant alternatives, as well as the demonstration of various applications.

3.1 Work Completed

The preliminary results in this proposal are contained in [29,39], where we introduced this method of model-based filtering for tractography using compact directional functions. Our preliminary results indicate that these filter-based approaches to tractography provide superior results compared to independent streamline estimation.

3.2 Work Remaining

There are several phases defining the remainder of this thesis:

1. Efforts thus far have focused on using Watson directional functions to model the local diffusion. To show the flexibility and stability of this filtering framework, we will apply this same methodology to incorporate Gaussian tensor models which will require additional parameters introducing further nonlinearities.
2. The next phase of this thesis will then focus on weighted mixtures for further flexibility in modeling partial volumes.
3. We have introduced a framework for fitting a diffusion model at a particular voxel based on the local signal. However, our experience suggests that it is important to take into account information beyond the local signal. Along those lines, various global techniques have been proposed to estimate entire paths at

once [13, 24, 41]; although, these focus on full connecting path and not accurate estimation of the local diffusion model. Our goal here is to develop a hybrid solution: local filtering for model estimation combined with global filtering for path estimation. For example, instead of estimating a local principle diffusion direction at each point, one could estimate an underlying curve to match the fiber geometry beyond a single voxel [33].

4. We begin validation on a physical phantom [37].
5. We will deliver a version of this algorithm as a Slicer module (<http://www.slicer.org>).
6. The final phase of this thesis will entail applying these techniques in the context of a population study where we study the effect of local model choice, *e.g.* single- or two-tensor models. Borrowing from our earlier work on nonparametric density estimation of manifold data [28], we will explore the suitability of this same modeling technique to the analysis of tractography data among individuals and groups.

The completion of this thesis requires the use of a computer, a MATLAB license, 3D Slicer, and access to diffusion MRI from patients—all currently available through Georgia Tech and our collaborations. We expect this work to be ready for presentation in Summer 2010.

REFERENCES

- [1] ALEXANDER, A., HASAN, K., TSURUDA, J., and PARKER, D., “Analysis of partial volume effects in diffusion-tensor MRI,” *Magnetic Resonance in Medicine*, vol. 45, pp. 770–780, 2001.
- [2] ALEXANDER, D. C., “Multiple-fiber reconstruction algorithms for diffusion MRI,” *Annals of the New York Academy of Sciences*, vol. 1046, no. 1, pp. 113–133, 2005.
- [3] ALEXANDER, D. C., BARKER, G., and ARRIDGE, S., “Detection and modeling of non-Gaussian apparent diffusion coefficient profiles in human brain data,” *Magnetic Resonance in Medicine*, vol. 48, pp. 331–340, 2002.
- [4] ANDERSON, A., “Measurement of fiber orientation distributions using high angular resolution diffusion imaging,” *Magnetic Resonance in Medicine*, vol. 54, no. 5, pp. 1194–1206, 2005.
- [5] ANWANDER, A., DESCOTEAUX, M., and DERICHE, R., “Probabilistic Q-Ball tractography solves crossings of the callosal fibers,” in *Human Brain Mapping*, p. 342, 2007.
- [6] BASSER, P., PAJEVIC, S., PIERPAOLI, C., DUDA, J., and ALDROUBI, A., “In vivo fiber tractography using DT-MRI data,” *Magnetic Resonance in Medicine*, vol. 44, pp. 625–632, 2000.
- [7] BEHRENS, T., JOHANSEN-BERG, H., JBABDI, S., RUSHWORTH, M., and WOOLRICH, M., “Probabilistic diffusion tractography with multiple fibre orientations: What can we gain?,” *NeuroImage*, vol. 34, pp. 144–155, 2007.
- [8] BJÖRNEMO, M., BRUN, A., KIKINIS, R., and WESTIN, C.-F., “Regularized stochastic white matter tractography using diffusion tensor MRI,” in *Medical Image Computing and Computer Assisted Intervention (MICCAI)*, pp. 435–442, 2002.
- [9] DERICHE, R., CALDER, J., and DESCOTEAUX, M., “Optimal real-time Q-Ball imaging using regularized Kalman filtering with incremental orientation sets,” *Medical Image Analysis*, vol. 13, no. 4, pp. 564–579, 2009.
- [10] DESCOTEAUX, M., ANGELINO, E., FITZGIBBONS, S., and DERICHE, R., “Regularized, fast, and robust analytical Q-ball imaging,” *Magnetic Resonance in Medicine*, vol. 58, pp. 497–510, 2007.

- [11] DESCOTEAUX, M., DERICHE, R., and ANWANDER, A., “Deterministic and probabilistic Q-ball tractography: from diffusion to sharp fiber distributions,” *Tech. Rep.* 6273, INRIA, 2007.
- [12] DESCOTEAUX, M., DERICHE, R., KNOESCHE, T., and ANWANDER, A., “Deterministic and probabilistic tractography based on complex fiber orientation distributions,” *Trans. on Med. Imag.*, vol. 28, no. 2, pp. 269–286, 2009.
- [13] FILLARD, P., POUPEON, C., and MANGIN, J.-F., “A novel global tractography algorithm based on an adaptive spin glass model,” in *Medical Image Computing and Computer Assisted Intervention (MICCAI)*, pp. 927–934, 2009.
- [14] FRANK, L., “Characterization of anisotropy in high angular resolution diffusion-weighted MRI,” *Magnetic Resonance in Medicine*, vol. 47, pp. 1083–1099, 2002.
- [15] GÖSSL, C., FAHRMEIR, L., PUTZ, B., AUER, L., and AUER, D., “Fiber tracking from DTI using linear state space models: Detectability of the pyramidal tract,” *NeuroImage*, vol. 16, pp. 378–388, 2002.
- [16] GUO, W., ZENG, Q., CHEN, Y., and LIU, Y., “Using multiple tensor deflection to reconstruct white matter fiber traces with branching,” in *Int. Symp. on Biomedical Imaging*, pp. 69–72, 2006.
- [17] HAGMANN, P., REESE, T., TSENG, W.-Y., MEULI, R., THIRAN, J.-P., and WEDEEN, V. J., “Diffusion spectrum imaging tractography in complex cerebral white matter: An investigation of the centrum semiovale,” in *Int. Symp. on Magnetic Resonance in Medicine (ISMRM)*, p. 623, 2004.
- [18] HESS, C., MUKHERJEE, P., HAN, E., XU, D., and VIGNERON, D., “Q-ball reconstruction of multimodal fiber orientations using the spherical harmonic basis,” *Magnetic Resonance in Medicine*, vol. 56, pp. 104–117, 2006.
- [19] HOSEY, T., WILLIAMS, G., and ANSORGE, R., “Inference of multiple fiber orientations in high angular resolution diffusion imaging,” *Magnetic Resonance in Medicine*, vol. 54, pp. 1480–1489, 2005.
- [20] JANSONS, K. and ALEXANDER, D. C., “Persistent angular structure: New insights from diffusion MRI data,” *Inverse Problems*, vol. 19, pp. 1031–1046, 2003.
- [21] JIAN, B. and VEMURI, B., “A unified computational framework for deconvolution to reconstruct multiple fibers from diffusion weighted MRI,” *Trans. on Med. Imag.*, vol. 26, no. 11, pp. 1464–1471, 2007.
- [22] JULIER, S. and UHLMANN, J., “Unscented filtering and nonlinear estimation,” *IEEE*, vol. 92, no. 3, pp. 401–422, 2004.

- [23] KADEN, E., KNØSCHE, T., and ANWANDER, A., “Parametric spherical deconvolution: Inferring anatomical connectivity using diffusion MR imaging,” *NeuroImage*, vol. 37, pp. 474–488, 2007.
- [24] KREHER, B., MADEER, I., and KISELEV, V., “Gibbs tracking: A novel approach for the reconstruction of neuronal pathways,” *Magnetic Resonance in Medicine*, vol. 60, pp. 953–963, 2008.
- [25] KREHER, B., SCHNEIDER, J., MADER, I., MARTIN, E., HENNIG, J., and IL’YASOV, K., “Multitensor approach for analysis and tracking of complex fiber configurations,” *Magnetic Resonance in Medicine*, vol. 54, pp. 1216–1225, 2005.
- [26] KUMAR, R., BARMPOUTIS, A., VEMURI, B. C., CARNEY, P. R., and MARECI, T. H., “Multi-fiber reconstruction from DW-MRI using a continuous mixture of von Mises-Fisher distributions,” in *Mathematical Methods in Biomedical Image Analysis (MMBIA)*, pp. 1–8, 2008.
- [27] LEFEBVRE, T., BRUYNINCKX, H., and SCHUTTER, J. D., “Kalman filters for non-linear systems: a comparison of performance,” *International Journal of Control*, vol. 77, no. 7, pp. 639–653, 2004.
- [28] MALCOLM, J., RATHI, Y., and TANNENBAUM, A., “A graph cut approach to image segmentation in tensor space,” in *Component Analysis Methods (in CVPR)*, pp. 1–8, 2007.
- [29] MALCOLM, J. G., MICHAILOVICH, O., BOUIX, S., WESTIN, C.-F., SHENTON, M. E., and RATHI, Y., “A filtered approach to neural tractography using the Watson directional function,” *Medical Image Analysis*. Accepted.
- [30] MALLAT, S. and ZHANG, Z., “Matching pursuits with time-frequency dictionaries,” *Trans. on Signal Processing*, vol. 41, pp. 3397–2415, 1993.
- [31] McGRAW, T., VEMURI, B., YEZIERSKI, B., and MARECI, T., “Von Mises-Fisher mixture model of the diffusion ODF,” in *Int. Symp. on Biomedical Imaging*, pp. 65–68, 2006.
- [32] ÖZARSLAN, E., SHEPHERD, T., VEMURI, B., BLACKBAND, S., and MARECI, T., “Resolution of complex tissue microarchitecture using the diffusion orientation transform,” *NeuroImage*, vol. 31, no. 3, pp. 1086–1103, 2006.
- [33] P. SAVADJIEV, S. W. Z. . K. S., “On the differential geometry of 3D flow patterns: Generalized helicoids and diffusion MRI analysis,” in *Int. Conf. on Computer Vision*, 2007.
- [34] PARKER, G. and ALEXANDER, D. C., “Probabilistic Monte Carlo based mapping of cerebral connections utilizing whole-brain crossing fiber information,” in *Information Processing in Medical Imaging (IPMI)*, pp. 684–696, 2003.

- [35] PARKER, G. and ALEXANDER, D. C., “Probabilistic anatomical connectivity derived from the microscopic persistent angular structure of cerebral tissue,” *Phil. Trans. R. Soc. B*, vol. 360, pp. 893–902, 2005.
- [36] PELED, S., FRIMAN, O., JOLESZ, F., and WESTIN, C.-F., “Geometrically constrained two-tensor model for crossing tracts in DWI,” *Magnetic Resonance in Medicine*, vol. 24, no. 9, pp. 1263–1270, 2006.
- [37] POUPON, C., RIEUL, B., KEZELE, I., PERRIN, M., POUPON, F., and MANGIN, J. F., “New diffusion phantoms dedicated to the study and validation of high-angular-resolution diffusion imaging (HARDI) models,” *Magnetic Resonance in Medicine*, vol. 60, no. 6, pp. 1276–83, 2008.
- [38] POUPON, C., ROCHE, A., DUBOIS, J., MANGIN, J.-F., and POUPON, F., “Real-time MR diffusion tensor and Q-ball imaging using Kalman filtering,” *Medical Image Analysis*, vol. 12, no. 5, pp. 527–534, 2008.
- [39] RATHI, Y., MALCOLM, J., BOUIX, S., WESTIN, C.-F., KUBICKI, M., and SHENTON, M. E., “Mixture model for estimating fiber ODF and multi-directional tractography,” in *Int. Symp. on Magnetic Resonance in Medicine (ISMRM)*, p. 3548, 2009.
- [40] RATHI, Y., MICHAILOVICH, O., SHENTON, M. E., and BOUIX, S., “Directional functions for orientation distribution estimation,” *Medical Image Analysis*, vol. 13, pp. 432–444, 2009.
- [41] REISERT, M., MADER, I., and KISELEV, V., “Global reconstruction of neuronal fibres,” in *Diffusion Modeling and Fiber Cup (in MICCAI)*, pp. 70–81, 2009.
- [42] SCHULTZ, T. and SEIDEL, H., “Estimating crossing fibers: A tensor decomposition approach,” *Trans. on Visualization and Computer Graphics*, vol. 14, no. 6, pp. 1635–1642, 2008.
- [43] TOURNIER, J.-D., CALAMANTE, F., and CONNELLY, A., “Robust determination of the fibre orientation distribution in diffusion MRI: Non-negativity constrained super-resolved spherical deconvolution,” *NeuroImage*, vol. 35, pp. 1459–1472, 2007.
- [44] TOURNIER, J.-D., CALAMANTE, F., GADIAN, D., and CONNELLY, A., “Direct estimation of the fiber orientation density function from diffusion-weighted MRI data using spherical deconvolution,” *NeuroImage*, vol. 23, pp. 1176–1185, 2004.
- [45] TUCH, D., “Q-ball imaging,” *Magnetic Resonance in Medicine*, vol. 52, pp. 1358–1372, 2004.
- [46] TUCH, D., REESE, T., WIEGELL, M., MAKRIS, N., BELLIVEAU, J., and WEDEEN, V., “High angular resolution diffusion imaging reveals intravoxel white matter fiber heterogeneity,” *Magnetic Resonance in Medicine*, vol. 48, pp. 577–582, 2002.

- [47] VAN DER MERWE, R. and WAN, E., “Sigma-point Kalman filters for probabilistic inference in dynamic state-space models,” in *Workshop on Advances in Machine Learning*, 2003.
- [48] ZHAN, W. and YANG, Y., “How accurately can the diffusion profiles indicate multiple fiber orientations? A study on general fiber crossings in diffusion MRI,” *J. of Magnetic Resonance*, vol. 183, pp. 193–202, 2006.
- [49] ZHANG, F., HANCOCK, E., GOODLETT, C., and GERIG, G., “Probabilistic white matter fiber tracking using particle filtering and von Mises-Fisher sampling,” *Medical Image Analysis*, vol. 13, pp. 5–18, 2009.
- [50] ZHUKOV, L. and BARR, A., “Oriented tensor reconstruction: Tracing neural pathways from diffusion tensor MRI,” in *Visualization*, pp. 387–394, 2002.